

Quasi Class-DE Driving of HIFU Transducer Arrays

Carlos Christoffersen, *Senior Member, IEEE*, Think Ngo, Ruiqi Song, Yushi Zhou *Member, IEEE*, Samuel Pichardo, and Laura Curiel, *Senior Member, IEEE*

Abstract—Recently a method was proposed to determine the parameters for each Class DE driver in high-intensity focused ultrasound (HIFU) arrays for efficient operation and to compensate for variations in the impedance of each array element. This work extends that method to consider the effect of switch resistance and to provide limited control on the power delivered to the transducers with a constant supply voltage while keeping a good efficiency. The method is experimentally validated using an integrated driver developed by the authors. This paper also shows that the frequency range for efficient electrical operation is close to the frequency where the transducer array presents a peak in the conversion efficiency.

Index Terms—Biomedical electronics, Class DE amplifier, Ultrasound transducer, HIFU

I. INTRODUCTION

INTEGRATED class DE amplifiers without inductors have been proposed as a compact solution to drive arrays of piezoelectric ultrasound transducers for HIFU therapy [1]–[3]. HIFU is a non-invasive surgical technique that thermally ablates tissue in human organs without the need of incision. Tissue ablation is achieved by focusing acoustic energy that translates into heat energy delivered to the focal zone of the ultrasound transducer [4], [5]. Frequently HIFU operation is guided by Magnetic Resonance Imaging (MRI) [6], which provides high contrast volumetric information and real-time monitoring of thermal effects. A multi-element ultrasound transducer array is required in order to electronically steer the focal zone. This is achieved by exciting all transducers at the same power level and adjusting the phase of each element. Several drivers for piezoelectric ultrasound transducers require external matching networks containing inductors [7]–[12]. These matching network circuits would interfere with the MRI-guidance system, so they cannot be used within the bore. Other proposed designs do not require inductors [13]–[17] but efficiency is not one of the main considerations in these designs and thus they tend to achieve lower efficiencies.

Drivers that operate in Class-DE mode [2], [3] may achieve higher efficiency without the need for inductors or transformers. The design presented in [2] achieved an output power of 830 mW, with an efficiency over 90%. In order to deliver

more power at the output, a full-bridge Class-DE amplifier [3] was also designed. Class DE operation as proposed here only requires a driver with a push-pull switch (or equivalent), an optional external capacitor and fine control on the duty cycle. For that reason, the technique presented in this work could be used to allow commercially available ultrasound pulsers normally intended for imaging applications (References [18]–[20] are some examples) to be used for HIFU, by reducing thermal dissipation on the chip. The driving frequency for ultrasound transducers is usually set at the series resonant frequency as this ensures that the input voltage is fully applied to the equivalent resistor in the series resonant branch [10]. However, this frequency does not take advantage of the loss reduction mechanism in the transducer, which occurs between the series and parallel resonance frequency range when the input impedance is inductive. It is shown in [10] that the mechanical efficiency of the transducer peaks between these two frequencies. When transducers are driven at a frequency in this range, they require less electrical power to produce the same mechanical output vibration. As this is the same frequency range where Class DE driving mode is feasible, our proposed approach has the potential to simultaneously achieve good efficiency on both transducer and driver.

When a transducer array is considered, the excitation frequency is common for all transducers but the individual duty cycle and external capacitor for each transducer must be adjusted to compensate for variations in the impedance of each array element. Recently, a technique to determine efficient driving parameters for an entire array was proposed in [1]. However, that method does not provide a means to control the power delivered by each transducer. Often transducer arrays require equal power on all elements [21]. This need comes from the fact that the prediction of the lesion shape relies on this assumption, so deviating from it, will cause an unwanted change in the lesion shape. This paper improves the analysis of the amplifier efficiency and extends the previously proposed method to allow for limited control of the power delivered to each transducer using the same supply voltage for all drivers. This is achieved by selecting the array excitation frequency, individual duty cycles and capacitive matching networks for each transducer.

II. SYSTEM MODELLING AND ANALYSIS

A. Transducer Array

This paper uses larger transducers with lower impedance than the ones used in [1]. This is to achieve a better efficiency with the driver [3] used for the experimental verification, which was originally designed for transducers of this size. The array is composed of six disc-shaped transducers with a

C. Christoffersen and Y. Zhou are with the Dept. of Electrical Engineering, Lakehead University, Canada. e-mail: c.christoffersen@ieee.org, yzhou30@lakeheadu.ca.

Think Ngo was with Lakehead University. He is now with Confederation College, Canada. e-mail: tngo@lakeheadu.ca

R. Song was with Lakehead University. He is now with Conavi Medical, 293 Lesmill Rd. North York, Ontario. e-mail: rsong1@lakeheadu.ca

S. Pichardo is with the Department of Radiology and Clinical Neurosciences, Hotchkiss Brain Institute Cumming School of Medicine, University of Calgary, Canada. e-mail: samuel.pichardo@ucalgary.ca

L. Curiel is with the Dept. of Electrical and Computer Engineering, University of Calgary, Canada. e-mail: laura.curiel@ucalgary.ca

TABLE I
TRANSDUCER PARAMETERS PARALLEL ABSORBER

Transducer	A	B	C	D	E	F
f_S (kHz)	998	1000	1002	999	1005	1003
f_P (kHz)	1106	1106	1109	1105	1114	1111
C_0 (pF)	557	545	665	619	622	521
C_S (pF)	130	125	156	145	148	121
L_S (μ H)	195	203	162	175	170	208
R_S (Ω)	40	41	43	47	41	39
Q_S	31	31	24	23	26	34

TABLE II
TRANSDUCER PARAMETERS 45° ABSORBER

Transducer	A	B	C	D	E	F
f_S (kHz)	998	1000	1002	997	1005	1003
f_P (kHz)	1106	1106	1110	1106	1113	1111
C_0 (pF)	561	493	739	696	527	638
C_S (pF)	132	112	178	150	122	151
L_S (μ H)	192	226	142	170	205	167
R_S (Ω)	40	42	43	49	42	39
Q_S	30	34	20	19	31	26

diameter of 20 mm and a thickness of 2.8 mm made of piezo-composite crystal [22]. Using a vector network analyzer, two characterizations were performed to consider variations in the acoustic environment: one with absorber material parallel to the transducer surface (Table I) and another with the absorber material at an angle of 45° (Table II). The series and parallel resonance frequencies are denoted f_S and f_P , respectively. The Q factor of the series resonant branch ($Q_S = \omega L_S / R_S$) at 1 MHz is also shown in the tables. The transducers used in this work have a high Q_S and reject frequencies far from the resonance.

The transducer conversion efficiency, defined as the ratio between the acoustic power over the electrical power delivered to the transducer was also measured. The acoustic power of the transducers was measured using the radiation force method [23] with an absorber [24] placed at the bottom of a container filled with deionized-degassed water, and the transducer suspended 2 cm away from the absorber. The container was placed on an analytical scale [25] with the transducer surface parallel to the absorber. Fig. 1 shows the acoustic power as a function of electrical input power for Transducer A at $f = 1040$ kHz. Circles represent measured points and the slope of the dashed line is the conversion efficiency, which was determined using least squares. Similar power sweeps were performed at different frequencies for all transducers. Fig. 2 shows the variation of the conversion efficiency with frequency for each transducer and also for the entire array under the assumption that all transducers receive the same electrical power. The efficiency peak happens between f_S and f_P at a frequency near 1040 kHz, with an average array efficiency of 77.6%.

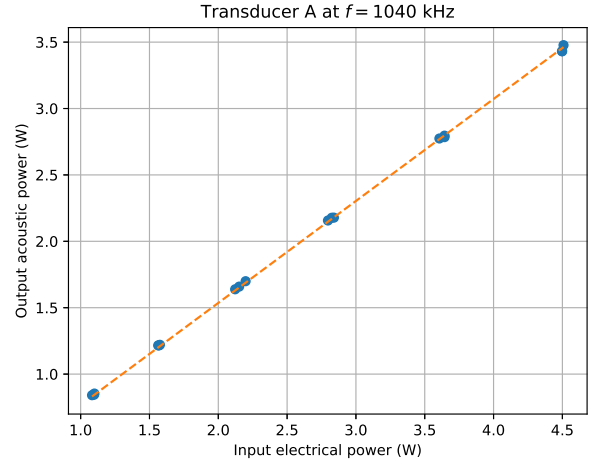


Fig. 1. Acoustic power as a function of electrical input power for Transducer A at $f = 1040$ kHz.

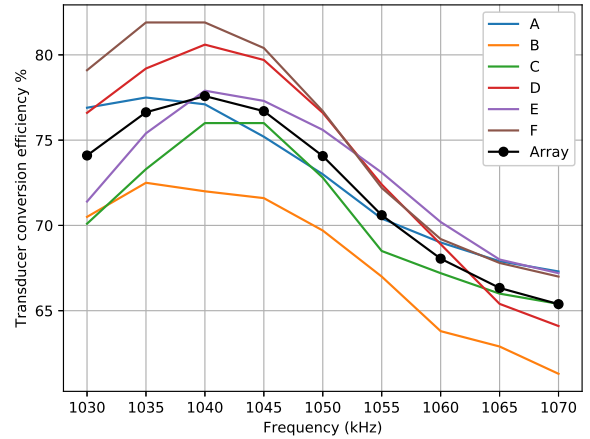


Fig. 2. Transducer conversion efficiency as a function of frequency.

B. Amplifier Analysis

Fig. 3 shows a simplified schematic diagram of a class DE amplifier. The parallel capacitor,

$$C_p = C_0 + C_{SW} + C_{ext} ,$$

includes the transducer parallel capacitor (C_0), the parasitic capacitance of the switches (C_{SW}) and any additional external capacitance (C_{ext}). For proper Class DE operation, the driver must be physically close to the transducer as explained in [2] to minimize the transmission line effect between the three components of C_p . In order to regulate the load power while keeping a constant supply voltage, we relax the zero voltage switching (ZVS) condition in the Class DE amplifier. This introduces switching losses but if the voltage drop at the switching instant is not too high, the overall efficiency remains reasonably high. We retain the zero derivative switching (ZDS) condition to keep a low sensitivity respect to small variations in the duty cycle and other circuit parameters. The operation of the Class DE amplifier has been analyzed in several papers,

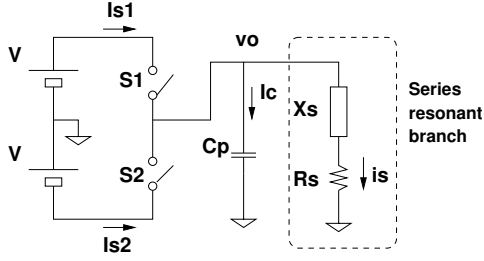


Fig. 3. Simplified schematic of a class DE amplifier.

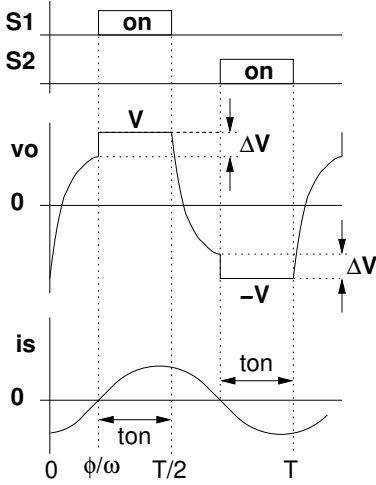


Fig. 4. Waveforms in class DE amplifier outside optimum conditions [1].

[26]–[29] are some of the most relevant examples. However, the analysis in the literature is focused in the most common case where there is an external RLC matching network. The analysis presented in this section is not available elsewhere. Fig. 4 shows the waveforms in the class DE amplifier under the considered non ideal conditions. The duty cycle (D) is defined as follows:

$$D = \frac{t_{on}}{T},$$

where t_{on} is the conduction time and T is the period of the excitation. The switches are operated with a duty cycle between 0 and 0.5, usually close to 0.25. The conduction angle (ϕ) is related to D by the following equation:

$$\phi = \pi(1 - 2D). \quad (1)$$

The voltage difference at the switch at the turn-on instant is denoted as ΔV . If the ZVS condition is satisfied, $\Delta V = 0$ and there is no switching loss.

1) *Series Branch Impedance Condition:* We now determine the series resonance branch (Fig. 3) impedance condition for quasi Class DE operation with $\Delta V \neq 0$, using similar steps used to analyze ideal Class DE operation in [26]. This analysis is based on the following assumptions [26]–[29]: (1) voltage drop in switch resistance is negligible, (2) capacitors are linear and lossless, (3) Q_S is high enough to assume underdamped regime, (4) higher harmonics of the current are neglected and (5) if $\Delta V \neq 0$, when the switch is turned on C_P charges to the supply voltage value in a negligible time as shown in

Fig. 4. The switch resistance normally is much lower than the load impedance. In practice this resistance produces a small voltage drop in the output waveform with a consequent reduction on the output power. The approach taken here is to neglect the effect of this resistance in the shape of the waves to establish the series branch impedance condition but later consider its effect in power calculations. The second and third assumptions are reasonable for piezoelectric transducers as discussed in Section II-A. As it will be shown in Sections IV and V, the fourth assumption causes an acceptably small error. Assumption (5) can be verified in each case by comparing the slew-rate of the driver (loaded with C_0) with T .

Due to the the high value of Q_S , the current in the series branch is sinusoidal given by:

$$i_s = I_p \sin(\omega t - \phi), \quad (2)$$

where I_p is the peak value, $\omega = 2\pi/T$ and t is time. The average power delivered to the load (P_{L1}) is thus given by:

$$P_{L1} = \frac{1}{2} R_S I_p^2. \quad (3)$$

During the $[0, \phi/\omega]$ interval, the current is provided by C_P and satisfies:

$$i_s = -C_p \frac{dv_o}{dt}, \quad (4)$$

where v_o is the output voltage. Combining (2) and (4), integrating, and imposing the following boundary conditions:

$$v_o(t=0) = -V \quad (5)$$

$$v_o(t=\phi/\omega) = V - \Delta V, \quad (6)$$

the output voltage for $0 \leq t \leq \phi/\omega$ is found to be

$$v_o = \frac{I_p}{\omega C_p} \left[\cos(\omega t - \phi) - \cos \phi - \frac{1 - \cos \phi}{2 - \delta} \right], \quad (7)$$

where $\delta = \Delta V/V$ and the peak current is given by:

$$I_p = \frac{(2 - \delta)\omega C_p V}{1 - \cos \phi}. \quad (8)$$

The fundamental component of the output voltage (V_o) is now determined using Fourier analysis:

$$V_o = \frac{2}{T} \int_0^T v_o(t) \exp(-j\omega t) dt.$$

The required series branch impedance (Z_S) is obtained as the ratio of V_o and the phasor corresponding to i_s (I_s):

$$Z_S = R_S + jX_S = \frac{V_o}{I_s}.$$

The condition for ZDS is thus:

$$\omega C_p R_S = \frac{1 - \cos(2\phi) + \delta \left(\frac{3}{2} + \frac{\cos(2\phi)}{2} - 2 \cos \phi \right)}{(2 - \delta)\pi} \quad (9)$$

$$\omega C_p X_S = \frac{2\phi - \sin(2\phi)}{2\pi}. \quad (10)$$

This result is consistent with Eq. (5) in [26] when $\delta = 0$ (ZVS condition). The external capacitor (C_{ext}) can be used to

control the output power. If C_p increases, ϕ must be increased to satisfy Eq. (10); this results in a lower D and a consequent reduction in load power. As the right hand side of Eq. (10) has a maximum equal to 1 when $D \rightarrow 0$ (i.e., $\phi \rightarrow \pi$), the largest value of C_p that maintains quasi Class DE operation is given by $C_{p,max} = 1/(\omega X_S)$. Replacing this value in Eqs. (3), (8) and (9), the following lower bound on the load power (P_{L2}) is obtained:

$$P_{L2} = \frac{8R_S V^2}{(\pi R_S + 4X_S)^2}. \quad (11)$$

It is important to remark that P_{L2} is only valid if the ZDS condition is enforced and Assumption (5) holds, i.e., C_p charges instantly regardless of the duty cycle. In practice Assumption (5) no longer holds when $D \rightarrow 0$ and the lowest achievable power in this operation mode is somewhat higher than the value predicted by Eq. (11). Despite these limitations this bound is useful for a rough estimation of the range where power control using this approach is feasible.

2) *Load power reduction due to switch resistance:* We present here a new strategy to model the reduction in load power due to the switch resistance (R_{SW}). This reduction is approximated by defining an average load peak voltage (V_A),

$$V_A = V - R_{SW} I_A, \quad (12)$$

where I_A is the average current in the switch during the conduction interval. This approximation improves accuracy with a simple modification to the existing equations. The effective peak current (I_{pE}) is obtained by substituting V_A in place of V in Eq. (8):

$$I_{pE} = \frac{(2 - \delta)\omega C_p V_A}{1 - \cos \phi}. \quad (13)$$

The value of I_A is obtained by averaging the current in the series branch over the $[\phi, \pi]$ interval, by combining Eq. (2) and (13):

$$I_A = I_{pE} \left(\frac{1}{\pi - \phi} \right) \int_{\phi}^{\pi} \sin(\theta - \phi) d\theta. \quad (14)$$

From Eq. (12), (13) and (14), $V_A = V/(1 + k)$ is obtained, where k is given by:

$$k = \frac{(2 - \delta)R_{SW}\omega C_p(1 - \cos(\pi - \phi))}{(\pi - \phi)(1 - \cos \phi)}. \quad (15)$$

The effective load power (P_L) is then estimated to be:

$$P_L = \frac{1}{2} R_S I_{pE}^2 = \frac{P_{L1}}{(1 + k)^2}. \quad (16)$$

3) *Losses and efficiency:* The observed voltage difference at the switch at the turn-on instant must be recalculated as:

$$\Delta V = \delta V_A + (V - V_A) = \left(\frac{\delta + k}{1 + k} \right) V = \delta_E V, \quad (17)$$

where δ_E is the observed $\Delta V/V$ ratio. The average switching loss power (P_S) is estimated as follows [1]:

$$P_S = f C_p \delta_E^2 V^2, \quad (18)$$

where $f = 1/T$. The total power loss in the driver (P_D) also includes a term approximately proportional to the switching

frequency that accounts for power dissipated by gate drivers (P_G) and a term that accounts for resistive losses in switches (P_R), namely:

$$P_D = P_S + P_G + P_R. \quad (19)$$

Resistive losses are calculated by averaging the power dissipated by the effective switch current. From Eq. (2) and (13):

$$P_R = \frac{R_{SW}}{\pi} I_{pE}^2 \int_{\phi}^{\pi} [\sin(\theta - \phi)]^2 d\theta. \quad (20)$$

Solving the integral in (20) and combining with Eq. (16), the following expression is obtained:

$$P_R = \frac{R_{SW}}{R_S} P_L \left[1 - \frac{\phi}{\pi} + \frac{\sin(2\phi)}{2\pi} \right]. \quad (21)$$

Eq. (21) is almost equivalent to the expression obtained in [28], but Eq. (21) additionally accounts for the voltage reduction due to the switch resistance.

The overall array efficiency (η) is defined as the ratio between the total power sent to the transducers and the total power dissipated:

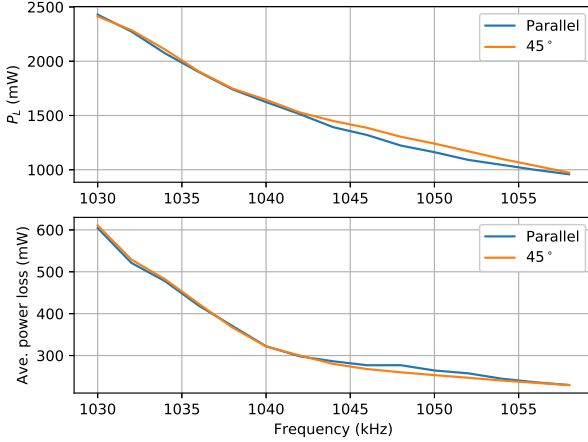
$$\eta = \frac{\sum P_L}{\sum (P_L + P_D)}. \quad (22)$$

III. PROPOSED METHOD

The objective of the method is to determine driver parameters, predict load power and losses in each amplifier and optionally provide control on the power of each individual transducer in the array while keeping the combined power efficiency in the array as high as possible. As an example, and for validation of the presented theory, the steps below show how to equalize the electrical power delivered to all transducers in the array. It is assumed that the switch capacitance is the same for all transducers, but C_0 may differ for each transducer. The method is composed of the following 5 steps:

- 1) Measure the transducer impedance (Z_T) of each element in the array in the frequency interval of interest. Determine the parallel capacitance C_0 for each transducer. The impedance of the series resonance branch is calculated as follows:
- $$Z_S = \frac{1}{\frac{1}{Z_T} - j\omega C_0}$$
- 2) For (non-optimum) Class DE operation, the operating frequency must be between the highest f_S and the lowest f_P for all transducers and it must be in the region where the series branch impedance is inductive. This is also the frequency range where transducer conversion efficiency peaks (Fig. 2). Based on these considerations, select a range for f .
 - 3) Set $C_{ext} = 0$ for all transducers. For each frequency in the considered range, numerically obtain ϕ for each transducer using Eq. (10) and use that value to solve for δ in Eq. (9):

$$\delta = \frac{2\pi\omega C_p R_S - 1 + \cos(2\phi)}{\pi\omega C_p R_S + \frac{3}{2} + \frac{\cos(2\phi)}{2} - 2\cos \phi}$$

Fig. 5. Load power (P_L) and average driver losses vs. frequency

If $\delta > 0$, the transducer can not be driven in ideal Class DE mode and the obtained value of ϕ corresponds to the best possible efficiency in sub-optimal mode. Else, if $\delta < 0$, C_{ext} must be increased to make $\delta = 0$. The value of C_{ext} is obtained by setting $\delta = 0$ and numerically solving for C_p and ϕ using Eq. (9) and (10). Calculate P_L for each transducer using Eq. (16). Each of these values represents the maximum power that can be delivered to a transducer.

- 4) The power delivered to each transducer may be reduced up to near the value predicted by Eq. (11). For example, if the electrical power delivered to each transducer is to be equalized, take the minimum from the set of calculated load powers (P_{min}) and increase C_{ext} in all other transducers to make all load powers equal to P_{min} . This is achieved by simultaneously solving for k , C_p , ϕ and δ in the system of equations formed by combining Eq. (9), (10), (15) and (16).
- 5) Estimate final array power and efficiency using Eq. (22) and select the operating frequency.

Fig. 5 shows the load power and losses vs. frequency using the two sets of transducer characterization parameters, $V = 20$ V, $R_{SW} = 4.6$ Ω , $C_{SW} = 26$ pF and $P_G = 180$ mW (at 1 MHz). For a constant supply voltage, the power delivered to the transducer is greater near f_S and decreases as f_P is approached, but as losses are also greater near f_S , the efficiency of the driver peaks at an intermediate frequency, as seen in Fig. 6.

As the method relies on compact analytical expressions, it requires little computational cost, for example a run for the set of 6 transducers shown here takes less than 1 second on a desktop computer. Table III shows calculated parameters for each transducer at 1042 kHz for Steps 3, 4 and 5. In Step 3, the initial maximum load power for each transducer is calculated (minimum value shown in boldface). Before equalization, P_L has large variations with a maximum of 31% difference between transducers D and E. In Step 4, the load powers are equalized and the final values for D , C_{ext} and δ are

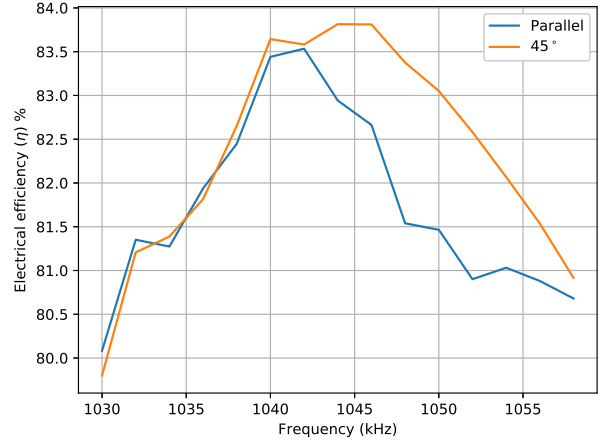
Fig. 6. Array electrical efficiency (η) vs. frequency.

TABLE III
CALCULATED PARAMETERS FOR EACH TRANSDUCER AT 1042 KHz

Step	Transducer	A	B	C	D	E	F
3	P_{L1} (mW)	1910	1636	2067	1626	2171	1886
	P_L (mW)	1767	1524	1896	1513	1983	1740
4	P_{L2} (mW)	816	715	891	718	935	819
	D (%)	24	26	21	25	20	23
	C_{ext} (pF)	574	308	817	284	1038	702
	δ	0.30	0.01	0.38	0.00	0.44	0.25
	δ_E	0.32	0.05	0.40	0.04	0.45	0.28
	P_L (mW)	1513	1513	1513	1513	1513	1513
5	P_D (mW)	288	253	335	255	375	282
	η_D (%)	84	86	82	86	80	84

obtained. In Step 5, losses and efficiency are calculated. The last row shows the electrical efficiency of each driver (η_D).

Fig. 7 shows individual driver efficiency as a function of P_L at 1042 kHz. This figure illustrates the control range and the trade-off between power control and efficiency using the proposed approach with the selected combination of driver and transducer. Powers could have been equalized at many levels, but it is clear from this figure that the greatest efficiency is obtained when they are equalized at the highest possible level as recommended in Step 4. It can also be observed in this figure that the control range with high efficiency is limited to cases where small power corrections are needed.

IV. SIMULATION RESULTS

The performance of the transducers in the array is evaluated by a steady-state simulation using an in-house circuit simulator which is freely available at <https://github.com/cechrist/cardoon>. The circuit topology is the same as shown in Fig. 3. Transducers are modelled using the measured scattering parameters in two different modes. In the first mode (Simulation 1), the scattering parameters with parallel absorber are used for the fundamental frequency response, for all other harmonics only the parallel capacitor of the lumped-element equivalent circuit is considered. This

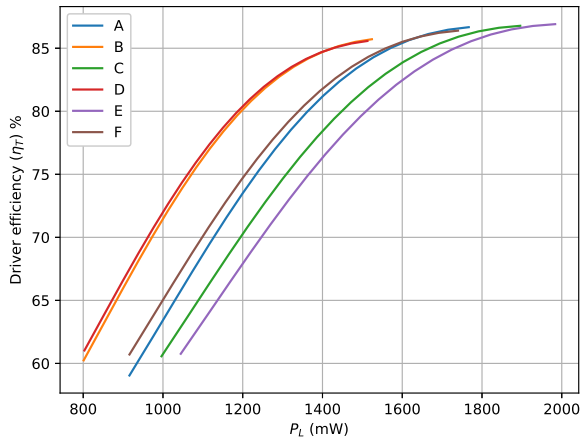


Fig. 7. Driver efficiency as a function of the load power (P_L) at 1042 kHz

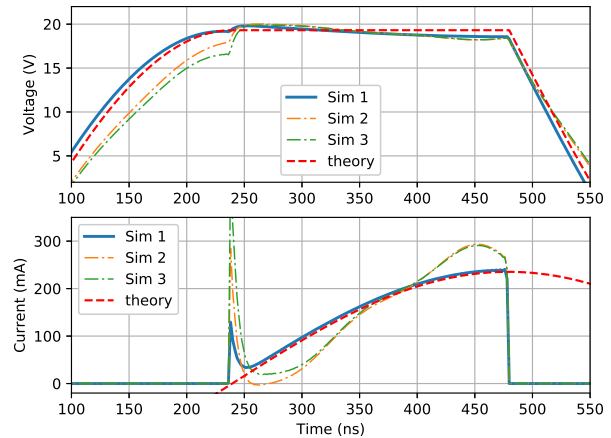


Fig. 9. Output voltage and current waveforms for Transducer D.

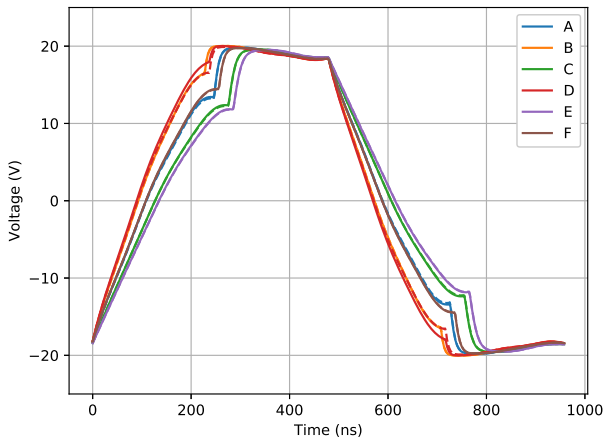


Fig. 8. Output voltage for all transducers using the accurate transducer model with parallel absorber (Sim. 2, continuous line) and with absorber placed at 45° (Sim. 3, dashed line).

mode removes the odd-harmonic secondary resonances from the transducer response. In the second mode (Simulations 2 and 3), the same approach is used but measured transducer parameters with parallel absorber and absorber at 45° , respectively, are used up to 10 MHz. Capacitor values have been adjusted to the nearest standard value for all simulations.

Fig. 8 shows all transducer voltages for Simulations 2 (continuous line) and 3 (dashed line). Differences between the two simulations are very small. The greatest difference is observed for Transducer D. Fig. 9 shows a detail of the voltage and current waves for the three simulations and the theoretical predicted waves for Transducer D. The upper graph shows the output voltage waves. The voltage drop due to the switch resistance, approximated as a constant drop in the theory analysis, can be observed. The lower graph shows the switch current waves for the three simulations and the analytically calculated wave for the series branch current (i_s). Tables IV and V summarize simulation results for P_L and

TABLE IV
SIMULATED OUTPUT POWER FOR EACH TRANSDUCER

Transducer	A	B	C	D	E	F
Predicted (mW)	1513	1513	1513	1513	1513	1513
Simulation 1 (mW)	1480	1469	1435	1493	1437	1475
Simulation 2 (mW)	1470	1398	1452	1410	1462	1459
Simulation 3 (mW)	1468	1400	1466	1509	1463	1464

δ_E , respectively. Both tables show good agreement between the simplified analytical analysis and simulation results. The main differences are that the simulated P_L is a little lower than the predicted value and sometimes δ_E is affected a little by the presence of harmonics in Simulations 2 and 3. As observed in Fig. 9, the currents have some oscillations that modify the value of δ_E . This effect is relatively small because the charge contributions of high frequency oscillations tend to compensate each other. For Simulation 1, the maximum difference in the obtained P_L is 4%. For Simulations 2 and 3, the average load powers are 1442 mW and 1463 mW, respectively and the maximum differences are 5% and 7%, respectively. Thus they are within the acceptable range (less than 10% [21]).

V. EXPERIMENTAL RESULTS

The six transducers were driven using the integrated driver described in [3]. This design is based on an H-bridge topology as shown in Fig. 10. Transistor dimensions in μm for M1 and M4 are: 360 fingers with $W/L = 50/1.4$, for M2 and M3: 140 fingers with $W/L = 50/1$. Transistors M1 and M2 in Fig. 10 operate in the same way as a half-bridge amplifier and transistors M3 and M4 operate with the complementary signals as indicated in the diagram. The integrated driver includes a logic control block to program duty ratio, phase shift and operating frequency. The driver was implemented using the AMS AG H35 CMOS process. A micrograph of the fabricated die including the I/O pads is shown in Fig. 11. Compared to the push-pull Class-DE amplifier shown in Fig. 3, the H-bridge Class-DE amplifier can deliver 4 times the output

TABLE V
SIMULATED δ_E FOR EACH TRANSDUCER

Transducer	A	B	C	D	E	F
Predicted	0.32	0.05	0.40	0.04	0.45	0.28
Simulation 1	0.33	0.09	0.41	0.04	0.45	0.28
Simulation 2	0.34	0.18	0.38	0.11	0.41	0.28
Simulation 3	0.34	0.18	0.39	0.17	0.41	0.28

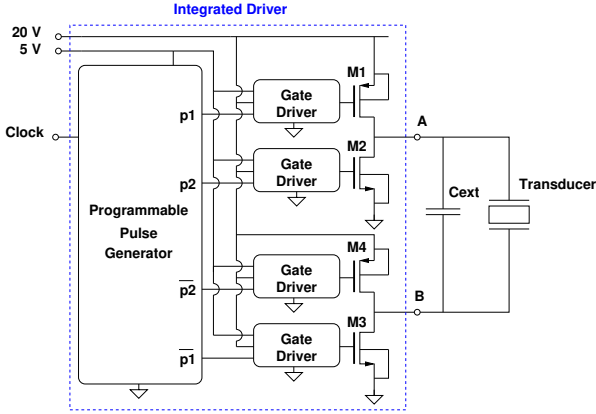


Fig. 10. Block diagram of the transducer driver

power with the same DC supply voltage. Another advantage is that the effective switch capacitance is divided by two as the capacitances on each side of the transducer appear as a series connection in parallel with the transducer load. These advantages come at the expense of double chip area to accommodate four transistors instead of two, additional power to drive its gates and double switch resistance. The equations presented in this paper are applicable to the H-bridge topology. For that case C_{SW} is defined as half the switch capacitance on each side of the H-bridge and R_{SW} is the sum of the resistances of two complementary transistors (M1 and M3, or M2 and M4).

The experimental setup used to obtain the measurements is shown in Fig. 12. A short section of coaxial cable was used to connect the transducers to the driver. The output voltage was measured as the difference between the two driver outputs referred to ground (nodes marked A and B in Figs. 10 and 12). The value of C_{SW} , including oscilloscope probes and parasitic capacitance from PCB and connectors was experimentally determined to be 26 pF. The supply voltage at the driver was set to 20 V. The driver was programmed to obtain duty cycles as close as possible to the values in Table III. The absorber was placed parallel to the transducer surfaces for all measurements. Table VI summarizes the experimental results. The measured values of the standard 5% capacitors used for C_{ext} are shown in this table. P_L in Table VI is the delivered power at the fundamental frequency and was calculated based on the experimentally measured load voltage and the previously measured reflection coefficient of the transducer as follows:

$$P_L = \frac{V_o^2}{2Z_0} \frac{1 - |\Gamma|^2}{|1 + \Gamma|^2},$$

where V_o is determined using Fourier analysis of the sampled

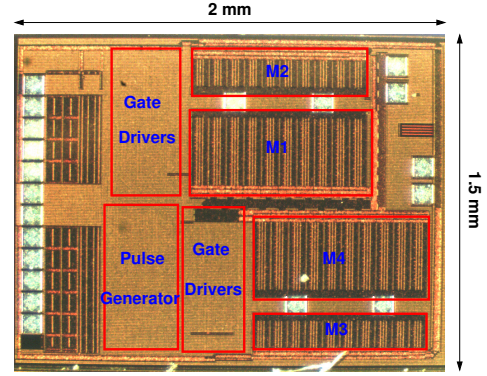


Fig. 11. Micrograph of the fabricated die

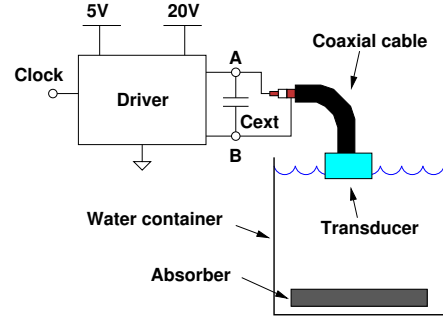


Fig. 12. Experimental setup for a single transducer

output voltage, Z_o is 50Ω and $\Gamma = (Z_T - Z_o)/(Z_T + Z_o)$. The value of η_D was obtained as the ratio between P_L and the DC power delivered to the driver (P_{DC}). The value of P_D was determined as the difference between P_{DC} and P_L . The experimental values of δ_E , P_L and η_D in Table VI show reasonably good agreement with the analytical predictions and simulations in Tables III, IV and V. The average transducer power in the array is 1366 mW, which is lower than the 1442 mW average predicted by simulations. One possible cause for this discrepancy is transducer impedance variation due to small environmental changes and other deviations from ideal conditions in the experimental setup. The experimental overall electrical efficiency for the array is 78%. Despite these discrepancies, the maximum difference in the measured P_L is 7 % between transducers A and D, which is within the expected range. The power at the third harmonic (P_3) was calculated in a similar way as the fundamental power. The third harmonic power level with this driving method is small and these results are consistent with previous measurements using a different transducer type [2]. Fig. 13 shows experimental (continuous line) and Simulation 2 output waveforms (dashed line) for all transducers. Good agreement is observed.

A. Magnetic resonance imaging compatibility

MR imaging was performed using a 3T MRI scanner (Achieva, Philips, Best, The Netherlands). Two transducers were placed inside a 1 L tank filled with deionized water, one for transmission connected to our driver and the other for reception to monitor the presence of an acoustic wave. An MR

TABLE VI
SUMMARY OF EXPERIMENTAL RESULTS

Transducer	A	B	C	D	E	F
D (%)	23.8	26.0	20.8	24.8	19.6	23.0
C_{ext} (pF)	527	328	838	273	953	704
δ_E	0.35	0.26	0.41	0.21	0.42	0.32
P_L (mW)	1412	1336	1380	1322	1398	1346
P_{DC} (mW)	1710	1660	1742	1758	1830	1740
P_D (mW)	298	324	362	436	432	394
η_D (%)	83	80	79	75	76	77
P_L/P_3 (dB)	32	26	32	25	31	32

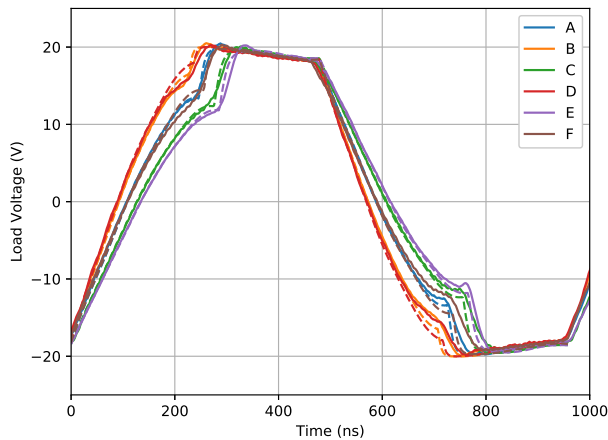


Fig. 13. Experimental output voltage for all transducers (continuous line) compared to Simulation 2 (dashed line).

bottle phantom (50 mL demineralized water with 11.55 mg of $\text{CuSO}_4 \cdot 5\text{H}_2\text{O}$, 0.015 ml of Arquad[®] at 1% and 0.00225 ml of $\text{H}_2\text{SO}_4 - 0.1\text{N}$) was placed next to the transducers. Spin Echo images and B1 maps were obtained using a head coil (Head Sense 8, Philips Healthcare). B1 mapping was calculated using a dual angle method ($\text{TE/TR} = 3.42/1036$ ms, $\text{FOV} = 30$ cm, slice thickness = 5 mm, flip angle $\alpha = 30^\circ$ and 60° , $\text{ETL} = 1$, $\text{NEX} = 1$). Spin Echo images ($\text{TE/TR} = 3.39/120$ ms, $\text{FOV} = 15$ cm, slice thickness = 5 mm, $\text{ETL} = 1$, $\text{NEX} = 1$) were obtained at different coronal slices across the phantom and transducers and they were used to calculate the signal to noise ratio (SNR) with and without the driver present. The SNR for each image was calculated as the ratio of the mean signal value in a 2×2 cm area at the center of the phantom divided by the standard deviation of a 2×2 cm matrix at the corner of the image where no signal was present. The average SNR for 5 images covering the transducers space was calculated for each of the conditions. The average SNR obtained without the driver present was 28.91 ± 2.23 dB. When the driver was present and connected to the transducers it was 27.33 ± 0.44 dB. Fig. 14 shows the spin echo images for those conditions at the coronal slice on the same plane as the driver was placed. The B1 maps for the two cases can be observed as well as the corresponding phase for the B1 maps. The change in SNR was not significant between the cases. B1 maps show uniformity and the image

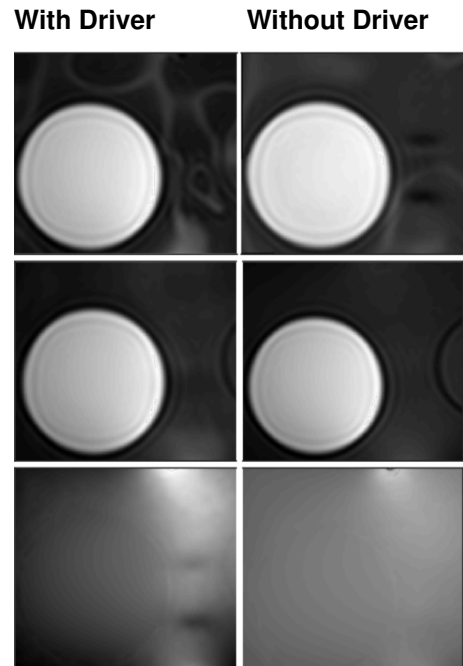


Fig. 14. Spin echo images (top), B1 map (middle) and B1 map phase images for the different conditions tested with the driver. The SNR was similar for all conditions and the B1 showed to be uniform.

is not affected by the presence of the driver.

This experiment was also used to verify that the driver is operational while in the MRI bore. At this time only operation while imaging is not active is being reported. As measuring instruments and power supplies can not be placed near the magnet, the driver was connected to the outside world through 7 m long transmission lines. The fundamental component of the voltage applied to the transducer was remotely measured as follows: one of the transmission lines was connected through 680Ω resistors in parallel with the load (points A and B in Fig. 10). The attenuation for the fundamental component of the load voltage at 1042 kHz was experimentally determined to be 0.27. Using this approach, the magnitude of the fundamental component of the voltage provided to Transducer A while the driver was operating in the bore was estimated to be 19.5 V. The acoustic signal was also detected by the receiver transducer, which was similarly connected to another transmission line.

VI. DISCUSSION

The analysis presented in this paper has been validated with the simulation and measurement of a transducer array. The overall performance obtained using the proposed approach is dependent on the driver, the transducer frequency response and the relative differences between transducers in the array. Table VII compares the performance obtained with the presented case study with other published integrated output stages for ultrasound transducers that provide efficiency data. The proposed approach is competitive, but performance with other transducer/driver combinations may vary.

To achieve reasonable output power levels and efficient operation when small transducers are considered, the driver

TABLE VII
TRANSDUCER DRIVER PERFORMANCE COMPARISON

Parameter	This work	[9]	[16]
Input voltage (V)	5	3.3	3.3
Output voltage (V)	20	± 4	20–50
Frequency (MHz)	1	1.5	10
Load Capacitance (pF)	> 1000	<i>LC</i> matching	15
Load Power (mW)	1366	560	130–160*
Power consumption (mW)	1740	800	545*
Efficiency (%)	78	70	24–29*

* Paper provides acoustic power data for 20 V supply voltage.

should be able to operate at high output voltages and present a low output capacitance. This is because small transducers tend to have a lower C_0 and a higher R_S . Small transducers also tend to have several close resonance frequencies because the thickness and the diameter may be comparable. For example, the transducers used in [1] have several resonance frequencies below or near 1 MHz: 305 kHz, 630 kHz, 870 kHz, 960 kHz, 1055 kHz and 1120 kHz. As demonstrated in [1], the transducers can operate in Class DE mode slightly above the 1055 kHz resonance. The transducers may also be operated at other resonance frequencies as long as a different transducer equivalent circuit characterization is performed for each resonance and the resulting equivalent circuit admits (quasi) Class DE operation.

If the transducers in the array are too different, it may not be possible to equalize all powers using this technique because the efficiency may become unacceptable or the required power for some transducers may fall below the bound predicted by Eq. (11). Ultimately, the acceptable efficiency is determined by how much power can be safely dissipated by the driver for a given package/thermal sink combination.

The use of a feedback system is still required to ensure correct acoustic power levels. A production system usually requires both acoustic and thermal sensors for each transducer [30]. Based on the data acquired by these sensors, the proposed method could be used to re-calculate the required duty cycles and external capacitor values to keep the system operating in optimum conditions. In this case the transducer impedance would have to be characterized at different temperatures and the goal of Step 4 must be set to equalize the power detected by the acoustic sensors. If unacceptable differences in the detected power remain after equalization (but still within the control range), the process could be iterated using ratio of the measured acoustic power and the calculated electric power as a scaling factor to improve accuracy. As an example, the parameters for acoustic power equalization are calculated using the parallel absorber transducer data and estimating the acoustic power (P_A) using the value of P_L and the measured conversion efficiency (Fig. 2). Fig. 15 shows the electrical efficiency (η) and the combined electrical-acoustic array efficiency, obtained using Eq. (22) but multiplying each term in the numerator by the corresponding transducer conversion efficiency. Table VIII shows the calculated driver parameters and expected performance at 1042 kHz. In this case, due to its lower conversion efficiency, Transducer B is set to provide

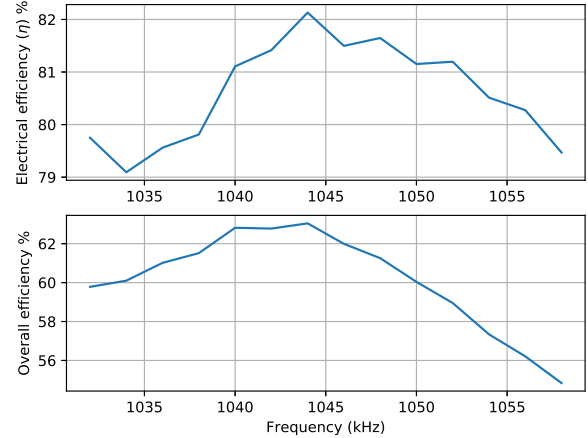


Fig. 15. Array electrical and overall efficiency vs. frequency.

TABLE VIII
CALCULATED PARAMETERS FOR EQUAL ACOUSTIC POWER AT 1042 KHZ

Transducer	A	B	C	D	E	F
D (%)	22	26	20	23	18	20
C_{ext} (pF)	690	295	927	473	1199	945
δ_E	0.39	0.03	0.45	0.20	0.52	0.42
P_L (mW)	1435	1524	1441	1365	1410	1348
P_A (mW)	1095	1095	1095	1095	1095	1095
L (mW)	312	254	365	255	428	332
η_D (%)	82	86	80	84	77	80

maximum power and the power in all other transducers is scaled back to perform the equalization.

VII. CONCLUSION

A method was presented to determine capacitive matching networks and driving parameters for an ultrasound transducer array operating the drivers in quasi class DE mode with limited power control capability. A set of analytical formulas to model the load power and losses in the driver was also presented. It was shown that for efficient operation at both the driver and the transducer, the array should be excited not at the transducer series resonance frequency but rather at an intermediate frequency between the series and parallel resonances. The proposed method is applicable to switching ultrasound drivers that allow precise duty cycle control. In this work, the method was experimentally verified using a full-custom driver to drive an array with equalized electrical power delivered to the transducers. Experimental results show an average power of 1366 mW in each transducer with a maximum power difference of 7% between transducers. The overall electrical system efficiency is 78%. Preliminary experiments indicate that the approach is compatible with MRI.

ACKNOWLEDGMENT

The authors would like to thank the National Research Council of Canada (NSERC) and CMC Microsystems for supporting this work.

REFERENCES

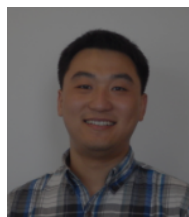
- [1] C. Christoffersen, T. Ngo, R. Song, Y. Zhou, S. Pichardo and L. Curiel, "Suboptimal Class DE Operation for Ultrasound Transducer Arrays," *Proceedings of the 2018 IEEE NEWCAS Conference*, Montreal, June 2018, pp. 1–4.
- [2] C. Christoffersen, W. Wong, S. Pichardo, G. Togtema and L. Curiel, "Class-DE Ultrasound Transducer Driver for HIFU Therapy," *IEEE Transactions On Biomedical Circuits And Systems*, Vol. 10, No. 2, April 2016, pp. 375–382.
- [3] R. Song, C. Christoffersen, Samuel Pichardo and Laura Curiel, "An integrated full-bridge Class-DE ultrasound transducer driver for HIFU applications," *Proceedings of the 2016 IEEE NEWCAS Conference*, Vancouver, June 2016, pp. 1–4.
- [4] Y. Ishihara, A. Calderon, H. Watanabe, K. Okamoto, Y. Suzuki, K. Kuroda and Y. Suzuki, "A precise and fast temperature mapping using water proton chemical shift," *Magnetic Resonance in Medicine*, vol. 34, no. 6, 1995, pp. 814–823.
- [5] P. Müller, A. Adam, "Principles of High-Intensity Focused Ultrasound," *International Oncology*, Springer, New York, 2012, pp. 51–63.
- [6] K. Hynynen, "MRI-guided focused ultrasound treatments," *Ultrasonics*, vol. 50, no. 2, 2010, pp. 221–229.
- [7] T. Hall and C. Cain, "A Low Cost Compact 512 Channel Therapeutic Ultrasound System For Transcutaneous Ultrasound Surgery," *AIP Conf. Proc.*, vol. 829, pp. 445–449, May 8 2006.
- [8] S. C. Tang and G. Clement, "A harmonic cancellation technique for an ultrasound transducer excited by a switched-mode power converter," *IEEE Trans. on Ultrasonics, Ferroelectrics and Frequency Control*, vol. 55, no. 2, pp. 359–367, February 2008.
- [9] W. T. Ang, C. Scurtescu, W. Wing Hoy, T. El-Bialy, Y. Y. Tsui and J. Chen, "Design and Implementation of Therapeutic Ultrasound Generating Circuit for Dental Tissue Formation and Tooth-Root Healing," *IEEE Trans. on Biomedical Circuits and Systems*, vol. 4, no. 1, pp. 49–61, Feb 2010.
- [10] T. Yuan, X. Dong, H. Shekhani, C. Li, Y. Maida, T. Toku and K. Uchino, "Driving an inductive piezoelectric transducer with class E inverter," *Sensors and Actuators A: Physical*, pp. 219–227, 2017.
- [11] H. Peng, J. Sabate, K. A. Wall, and J. S. Glaser, "GaN-Based High-Frequency High-Energy Delivery Transformer Push-Pull Inverter for Ultrasound Pulsing Application," *IEEE Trans. on Power Electronics*, vol. 33, no. 8, pp. 6794–6806, Aug. 2018.
- [12] H. D. Tiwari, K. Jae-Hyung and W. H. Cho, "Design and implementation of complete wearable low-intensity pulsed ultrasound therapeutic device," *Proc. of IEEE ISCAS 2018*, pp. 1–5, May 2018.
- [13] G. Lewis and W. Olbricht, "Design and characterization of a high-power ultrasound driver with ultralow-output impedance," *Rev. Sci. Instrum.*, vol. 80, no. 11, Nov. 2009.
- [14] A. Bozkurt, O. Farhanieh, R. B. Roy and A. S. Ergun, "Design of a driver IC for an ultrasound catheter ablation system," *Proc. of the 2014 IEEE Int. Ultrasonics Symp.*, pp. 1536–1539, Sept. 2014.
- [15] L. Capineri, "A 15 MHz bandwidth, 60 Vpp, low distortion power amplifier for driving high power piezoelectric transducers," *Review of Scientific Instruments*, Italy, AIP Publishing LLC, 2014.
- [16] O. Farhanieh, A. Sahafi, R. B. Roy, A. S. Ergun, and A. Bozkurt, "Integrated HIFU Drive System on a Chip for CMUT-Based Catheter Ablation System," *IEEE Trans. on Biomedical Circuits and Systems*, vol. 11, no. 3, pp. 536–546, June 2017.
- [17] A. Marzo, T. Corkett, and B. W. Drinkwater, "Ultrano: An Open Phased-Array System for Narrowband Airborne Ultrasound Transmission," *IEEE Trans. on Ultrasonics, Ferroelectrics, And Frequency Control*, vol. 65, no. 1, pp. 102–111, January 2018.
- [18] MAX4940, Dual/Qual, Unipolar/Bipolar, High-Voltage Digital Pulsers, Maxim Integrated, San Jose, CA, USA, 2009.
- [19] HV738, Four-Channel, High Speed, Ultrasound Pulser, Microchip Technology Inc., Chandler, AZ, USA, 2011.
- [20] LM96550 Ultrasound Transmit Pulser, Texas Instruments Inc., Dallas, TX, USA, 2010.
- [21] F. Dupenloup, J. Y. Chapelon, D. J. Cathignol and O. A. Sapozhnikov, "Reduction of the grating lobes of annular arrays used in focused ultrasound surgery," *IEEE Trans. on Ultrasonics, Ferroelectrics, and Frequency Control*, vol. 43, no. 6, pp. 991–998, 1996.
- [22] DL47, DeL Piezo, West Palm Beach, FL
- [23] Ultrasonics — Power measurement — Radiation force balances and performance requirements, IEC International Standard 61161, edition 3.0, Jan. 2013
- [24] Aptflex F28, Precision Acoustics, Dorset, United Kingdom
- [25] PI-225D, Denver Instrument, Bohemia, NY, USA
- [26] D. C. Hamill, "Impedance plane analysis of class DE amplifier," *Electronics Letters*, Vol. 30, Issue 23, pp. 1905–1906, Nov. 1994.
- [27] H. Sekiya, T. Negishi, T. Suetsugu and T. Yahagi, "Operation of class DE amplifier outside optimum condition," *Proc. of IEEE ISCAS 2006*, pp. 21–24, May 2006.
- [28] H. Sekiya, X. Wei, T. Nagashima and M. K. Kazimierczuk, "Steady-State Analysis and Design of Class-DE Inverter at Any Duty Ratio," *IEEE Trans. on Power Electronics*, vol. 30, no. 7, pp. 3685–3694, 2015.
- [29] L. Albertoni, F. Grasso, J. Matteucci, M. C. Piccirilli, A. Reatti, A. Ayachit and M. K. Kazimierczuk, "Analysis and design of full-bridge Class-DE inverter at fixed duty cycle," *Proc. of the 2016 42th IEEE Conf. on Industrial Electronics IECON*, pp. 5609–5614, 2016.
- [30] M. M. El-Desouki and K. Hynynen, "Driving circuitry for focused ultrasound noninvasive surgery and drug delivery applications," *Sensors*, no. 11, pp. 539–556, 2011.



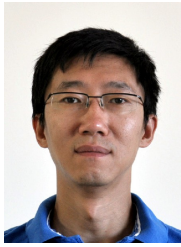
Carlos Christoffersen received the Electronic Engineer degree at the National University of Rosario, Argentina in 1993. From 1993 to 1995 he was research fellow of the National Research Council of Argentina (CONICET). He received an MSc degree and a PhD degree in electrical engineering in 1998 and 2000, respectively, from North Carolina State University (NCSSU). From 1996 to 2001 he was with the Department of Electrical and Computer Engineering at NCSSU. Since 2002 he is with the Department of Electrical Engineering at Lakehead University, Thunder Bay, Canada. He is currently an Associate Professor. Dr. Christoffersen's current research interests include ultrasound driver circuits and design and modelling of analog and RF circuits.



Think Ngo received B.E. and MSc. degrees in electrical engineering in 2016 and 2018, respectively, from Lakehead University. His research focused on ultrasound driver circuits. He is currently a college professor at Confederation College, Ontario.



Ruiqi Song received the B.E degree from Xi'an Technological University, Xi'an, China, in 2013, and the M.Sc degree from Lakehead University, Thunder Bay, Canada, specializing in analog circuit design and CMOS layout. His current interests are in the area of RF and ultrasound driver circuits. He is currently working in Conavi Medical Inc. as an Electrical Engineer.



Yushi Zhou received B.E.Sc. degree from University of Electronic Science and Technology of China, Chengdu, China, in 2000. From 2000 to 2008, he was a Senior ASIC Design Engineer with T3G Co., Ltd. (acquired by ST-Ericsson). He holds Ph.D. in electrical engineering from Ryerson University, Toronto, ON, Canada in 2015. From 2015 to 2016, he was with Semtech Corp., Toronto. Since 2016 he has been with the Department of Electrical Engineering, Lakehead University, Thunder Bay, where he is currently an Assistant Professor. His research

interests include low-power wireless receiver, HIFU driving circuits, and SerDes in high-speed communication.



Laura Curiel was born in Mexico City and received a degree in Electronic Systems Engineering from the Technologic Institute of Superior Studies of Monterrey, Mexico in 1995. She holds a PhD in Imaging and Systems from the National Institute of Applied Sciences in Lyon, France and a Masters degree from the University of Lyon. She is currently an Assistant Professor at the University of Calgary and an Adjunct Professor at Lakehead University. Her research interests center on development of HIFU therapeutic devices, novel imaging guidance

and interactions of ultrasound with tissues.



Samuel Pichardo received the B.E. degree in electronic systems from the Monterrey Institute of Technology and Higher Education, Mexico city, Mexico, in 1995, and the M.Sc. and Ph.D. degrees in Imaging and Systems from the National Applied Sciences Institute, Lyon, France, in 2001 and 2005, respectively. From 2008 to 2017, he worked as a Scientist at the Thunder Bay Regional Research Institute, Thunder Bay, Canada. In 2017, he joined the departments of Radiology and Clinical Neurosciences in the Cumming School of Medicine of the University of

Calgary, Canada, as Assistant Professor. He is also Adjunct Professor in the departments of Electrical Engineering and Physics at Lakehead University, Thunder Bay, Canada. His main areas of research are Magnetic Resonance Imaging-guided High Intensity Focused Ultrasound (MR-HIFU), transcranial ultrasound propagation, bioeffects of ultrasound, software tools for real time control of MR-HIFU, new devices and driving systems for ultrasound and interventional MRI.